# PARTICLE ENTRAINMENT AND NITRIC OXIDE REDUCTION IN THE FREEBOARD OF A FLUIDIZED COAL COMBUSTOR

P. M. Walsh, T. Z. Chaung, A. Dutta, J. M. Beér, and A. F. Sarofim

The Energy Laboratory and Department of Chemical Engineering
Massachusetts Institute of Technology, Cambridge, MA 02139

## 1.0 Introduction

Economic design of fluidized bed combustors requires a combination of fluidizing velocities and particle sizes which result in the unavoidable carry over of bed solids, coal char particles and unburned gaseous combustion products into the freeboard. Depending upon the design parameters, the last 5 to 10% of the combustibles will burn, and also significant reduction of $SO_2$ and $NO_x$ will take place in the freeboard of the fluidized combustor - between the top of the bed and the first row of the convective tube bank. Despite the importance of the freeboard to the efficient and clean operation of fluidized combustors, until recently little attention was paid to the understanding of the freeboard reactions. Pereira et al (1) and Gibbs et al (2) have determined chemical species concentration variation along the height of a 30 x 30 cm cross section fluidized bed and found that significant reduction of $NO_x$ takes place above the bed surface. Okada et al (3) have shown that the fine sorbent particles entrained into the freeboard will enhance sulfur capture and that the entrained char particles will react with $NO_x$ and reduce its emission.

In earlier designs of fluidized combustors the problem posed by unacceptably high carbon carry over at fluidizing velocities was resolved by the introduction of the fines precipitated from the flue gas into a "carbon burn-up cell," an uncooled fluidized bed operating at lower fluidizing velocity. In recent designs, instead of the carbon burn-up cell the method of fines reinjection into the fluidized bed is adopted. In order to achieve operational simplicity the fines in most practical applications are added to fresh feed and returned into the bed. Fines reinjection significantly increases the fine particle concentration in the bed and in the freeboard with the consequence of further enhancing the rate of the heterogeneous reactions of char oxidation, and $SO_2$ and $NO_x$ reduction in the freeboard.

Modeling of the freeboard reactions has been hindered by incomplete understanding of the processes which govern the entrainment of bed solid particles into the freeboard and the mixing of these solids with the reactant gas. Entrainment models by George and Grace (4), Wen and Chen (5) and Horio et al (6) have fulfilled an important role in predicting solids concentration in the freeboard, but due to a dearth of experimental information on entrainment rate as a function of the fluidization parameters of the bed, these models could not be rigorously tested and developed to the stage where they can be incorporated into FBC combustion models with sufficient confidence.

The importance of the NO-carbon reaction for the reduction of NO in fluidized combustion of coal was recognized and experimentally demonstrated by Pereira and Beér (7), Gibbs et al (2) and Furusawa et al (8). Kinetic parameters for this reaction were reported by Beér et al (9), Kunii et al (10) and Chan (11). Chan also found that the NO-char reaction can be significantly enhanced in the presence of CO.

The problems of predicting $NO_x$ reduction in the freeboard with sufficient accuracy are not only due to uncertainties about solids entrainment but also about the relative significance that CO, coal volatiles, volatile nitrogen compounds, or hydrocarbons may have on NO reduction (Sarofim and Beér (12), Yamazaki et al (13)). In recent experimental studies at MIT detailed hydrocarbon species concentration measurements by Walsh et al (14) have shown that CO and hydrocarbon concentrations are high in the "splash zone" immediately above the bed so that their effect on NO reduc-

tion in this region may not be neglected.

In the following, model calculations are presented of the reduction of NO along the height of the freeboard of the MIT 0.6 x 0.6m cross section, 4.5m high fluidized bed. In the model a new approach is made to the prediction of solids concentration in the freeboard (Chaung (15)) which is assisted by measurement data on the descending flux of particles. The NO reduction along the height above the bed is then predicted from experimental information on the carbon content of bed solids and the chemical kinetic rate equation on the NO-carbon reaction. The NO reductions so calculated are then compared with measurement data obtained burning bituminous and subbituminous coals in the 0.6 x 0.6m MIT experimental facility.

## 2.0 Particle Entrainment in the Freeboard

### 2.1 Theory of Particle Entrainment

A model has been developed for the entrainment of particles from the bed into the freeboard of a fluidized combustor. Its purpose is to provide an estimate of the total surface area of each solid species participating in chemical reactions in this zone. The model is based on the following assumptions:

1. Bursting bubbles eject particles into the freeboard.
2. Particle-particle interactions and wall effects are negligible.
3. The changes in mass and size of a particle due to chemical reaction while in the freeboard are negligible.
4. Interaction of the concentration, temperature, and velocity gradients surrounding each particle are negligible.
5. The initial velocities of particles ejected from the bed are given by a semi-empirical log-normal distribution having a geometric mean value proprotional to bubble velocity.
6. Bubble diameters are determined by the heat exchanger tube spacing and the bubble growth model of Mori and Wen (16).

The sequence of steps in the calculation of particle density (mass of particles/volume of gas-particle mixture) is as follows:

1. The initial velocities of the particles leaving the bed are given by the assumed semi-empirical velocity distribution.
2. The initial flux of particles is proportional to the flux of bubbles at the top of the bed. The proportionality factor is determined by equating the kinetic energies of a bursting bubble and the particles which it ejects.
3. The equation of motion is solved for each particle size and initial velocity to determine the particle trajectories.
4. The particle density is determined from the ratios of flux to velocity at each freeboard height. Total density is found by summing the contributions from all sizes and initial velocities.

Because solution of the equations of motion is time-consuming, for the required range of particle sizes and initial velocities, a simplified version of the model was also developed, based on two additional assumptions:

7. Small particles, having $u_t < u_g$, ascend with constant velocity, $v_s = u_g - u_t$.
8. The drag force is negligible on particles having $u_t \geq u_g$.

Chaung (15) showed that the deviation of the particle fluxes predicted by the two models was less than the uncertainty in the results of the more accurate version.

Detailed description of the essential features of the model.

Initial velocity distribution.

A log-normal fit was made to the distribution of ejected particle velocities given by George and Grace ( 4 ), which were normalized to the absolute bubble velocities, $u_b$. The geometric mean particle velocity and standard deviation were 2.44 $u_b$ and 1.43, respectively.

Initial Entrainment

George and Grace ( 4 ), defined a parameter, $\xi$, equal to the ratio of the volumes of entrained particles and bursting bubble. Using this parameter, the entrainment from the bed surface, $E_o$, can be expressed by

$$E_o = \xi\, Q_b\, \rho_s\, (1 - \varepsilon_{mf})\, A_t \qquad 1)$$

Glicksman et al. (17) give an expression for the visible bubble flow rate, $Q_b$, valid over the entire range of bubble volume fraction, $\delta$:

$$Q_b = u_g - (1 - \delta)\, [1 - \frac{\pi}{2}\, \ell n\, (1 - \frac{6\delta}{\pi})]\, u_{mf} \qquad 2)$$

The total energy of a bubble before bursting can be equated to the energy of the entrained particles and the energy of the bubble through-flow gas. The total energy of the bubble is given by the following equation from Davidson and Harrison (18):

$$(KE)_b = \frac{1}{2}\, m_{b,eff}\, u_b^2 \qquad 3)$$

where the effective mass of a bubble, $m_{b,eff}$, is

$$m_{b,eff} = \frac{1}{2}\ (\text{mass of fluid displaced by the bubble})$$

$$= \frac{2}{3}\, \pi\, R_b^3\, \rho_s\, (1 - \varepsilon_{mf}) \qquad 4)$$

Defining the root-mean-square velocity of the entrained particles as $\bar{v}_p$, the total kinetic energy of the particles ejected by the bubble is:

$$(KE)_p = \frac{1}{2}\, [\, \xi\, (\frac{4}{3}\, \pi R_b^3)\, \rho_s\, (1 - \varepsilon_{mf})]\, \bar{v}_p^2 \qquad 5)$$

where

$$\bar{v}_p = [\, \int v_p^2\, dm_p\,]^{1/2} \qquad 6)$$

The kinetic energy of bubble through-flow gas is approximately

$$(KE)_g \cong \frac{1}{2}\, [\rho_g\, \pi R_b^2\, (u_b + 3\, u_{mf})]\, (u_b + 3\, u_{mf})^2 \qquad 7)$$

which is usually negligible compared with $(KE)_b$ or $(KE)_p$. The energy balance, i.e., $(KE)_b \cong (KE)_p$, then yields:

$$\xi = \frac{u_b^2}{2\, \bar{v}_p^2} \qquad 8)$$

The absolute bubble velocity is given by

$$u_b = u_g - u_{mf} + 0.711\ (gd_b)^{1/2} \qquad 9)$$

The bubble diameter, $d_b$, at the top of the bed was found by assuming an initial diameter equal to the spacing of the heat exchanger tubes, and growth according the correlation of Mori and Wen (16). This result; with the assumed velocity distribution; Equations 2, 8, and 9; and the appropriate experimental data; provide the information required to calculate the initial entrainment by Equation 1. No assumption has been made regarding the source of the particles, i.e., whether they originate in the wake or the cap of a bubble.

Calculation of Particle Density

The equation of motion of the particles is

$$v_s \frac{dv_s}{dZ} = -\frac{3}{4} \frac{C_d \rho_g (v_s - u_g) |v_s - u_g|}{\rho_s d_p} - \frac{(\rho_s - \rho_g) g}{\rho_s} \qquad 10)$$

Subject to the initial conditions

$$v_s = v_{si} \text{ at } Z = 0 \qquad 11)$$

The total particle density profile along the freeboard is obtained by summing up all the contributions from ascending and descending particles.

$$\rho(Z) = \sum_{i} \sum_{j} \left[ \frac{E_u (d_{pi}, v_{sj})}{v_u (d_{pi}, v_{sj})} + \frac{E_d (d_{pi}, v_{sj})}{v_d (d_{pi}, v_{sj})} \right] \qquad 12)$$

(all particle sizes)

(all initial velocities)

The calculation must be repeated 6000 times if the particle size range is divided into 60 intervals and the initial velocity distribution into 100 intervals.

The Simplified Model

In order to save computer time the model was simplified by neglecting the transient term for small particles and the drag force term for large particles. The equations to be solved are then:

for small particles ($u_t < u_g$), $v_s = u_g - u_t$

for large particles ($u_t \geq u_g$), 13)

$$v_s \frac{d v_s}{dZ} = -\frac{(\rho_s - \rho_g) g}{\rho_s} \qquad 14)$$

which gives for ascending particles

$$v_s = \sqrt{v_{si}^2 - 2gZ \frac{(\rho_s - \rho_g)}{\rho_s}} \qquad 15)$$

The maximum height that a large particle can reach is

$$H_{max} = \frac{\rho_s v_{si}^2}{2(\rho_s - \rho_g)g} \qquad 16)$$

for descending particles

$$v_s = -\sqrt{2g\left(\frac{\rho_s-\rho_g}{\rho_s}\right)(H_{max}-Z)} = -\sqrt{v_{si}^2 - 2gZ\left(\frac{\rho_s-\rho_g}{\rho_s}\right)} \qquad 17)$$

Since the local velocity of each particle is obtained in analytic form, the particle density (Equation 12) yields a closed-form expression:

$$\rho(Z) = \int_{\sqrt{2gZ\,(\rho_s-\rho_g)/\rho_s}}^{\sqrt{2gH_f\,(\rho_s-\rho_g)/\rho_s}} \frac{2(1-y_c)E_o\, f_i dv_{si}}{\sqrt{v_{si}^2-2gZ(\rho_s-\rho_g)/\rho_s}} \quad \text{(Large particles not elutriacted)}$$

$$+ \int_{\sqrt{2gH_f(\rho_s-\rho_g)/\rho_s}}^{v_{si_{max}}} \frac{(1-y_c)E_o f_i dv_{si}}{\sqrt{v_{si}^2-2gZ(\rho_s-\rho_g)/\rho_s}} \quad \text{(Large particles elutriated)}$$

$$+ \int^{d_{pc}} \frac{y(dp)\cdot E_o \cdot d(dp)}{u_g\, u_t\,(dp)} \quad \text{(Small particles elutriated)} \qquad 18)$$

where $y_c = \sum^{o}_{u_t(d_{p_i}) < u_g} y(d_{p_i})$ is the mass fraction of small particles, and $f_i\, d\, v_{si}$ represents the mass fraction of particles with an initial velocity between $v_{si}$ and $v_{si} + dv_{si}$. The validity of the approximations made in simplifying the model was by comparing the particle densities predicted by the two methods (15). The maximum discrepancy was less than 30% of the particle density predicted by the complete model, and the significant features of both density profiles were identical. The results presented here were obtained using the simpler model.

Two Component Bed

When the bed has two components, for example a very small amount of char mixed with stone, the initial entrainment of the char, $E_{o,c}$, is a small fraction of the total initial entrainment. Assuming that the stratification factor is equal to the density ratio,

$$E_{o,c} = E_o \frac{\rho_s}{\rho_{s,c}}\, Y_c \qquad 19)$$

The initial velocity distribution for the char is the same as for the stone, and the total char density is found by the same procedure as before, with $\rho_{s,c}$ in place of $\rho_s$.

## 2.2 Measurement of Particle Flux

All of the experiments described in the present paper were performed using the M.I.T. Fluidized Combustion Research Facility, shown in Figure 1. The combustor has a square cross-section, 0.6m x 0.6m; and the total height, from distributor to exit, of 4.5m. The system has been described in detail elsewhere, (Beér et al. (19)).

The mass fluxes of particles extrained in the freeboard at various superficial gas velocities were measured in cold flow experiments by collecting descending particles at various heights above the surface of the fluidized bed. The particle collecting probe was formed by cutting a 22mm diameter tube in half lengthwise, so that it collects particles falling through a narrow strip on one axis of the combustor cross-section. The bed was a single batch of Ottawa Silica Sand (grade #20). Fine particles were removed from the bed by running for several hours prior to making the flux measurements. During the experiments attrition of bed particles and elutriation of fines were negligible. The bed particle size distribution had a geometric mean diameter of 720 $\pm$ 50μm, determined by sieve analysis. The bed was fluidized by ambient air supplied by forced-draft blowers. Bed temperature (average) and pressure (at the distributor) were 330 $\pm$ 20 K and 111 $\pm$ 2 kPa, respectively. Superficial velocity, calculated for the empty tude at the bed temperature and pressure, was varied from 0.42 to 0.86 m/s. The superficial velocity and void fraction at minimum fluidization were 0.37 $\pm$ 0.02 m/s and 0.50 $\pm$ 0.01, respectively.

For measurement of the particle fluxes, the probes were first oriented upside-down until steady bed conditions were achieved at the desired superficial velocity; the probe was then rotated to face upward and collect the descending particles. After sufficient time had elapsed to approximately half-fill the probe, the blowers were stopped, and the particles removed and weighed. Sampling times varied from 1 minute to 10 hours, depending on height and superficial velocity. The method relies upon the assumption that the paths of particles in the vicinity of the probe, moving either upward or downward, are not significantly affected by the motion of the gas around the probe.

## 2.3 Comparison of the Measured and Predicted Particle Flow Rates

The complete set of experimental particle flow data were reported by Mayo (20). An exponential decay of the particle flow rate with height was observed, having a characteristic length which increased with increasing gas velocity.

Some representative data points are shown in Figure 2, together with the corresponding flow rates calculated using the entrainment model. The predicted profiles show a small region of approximately constant particles flow rate just above the bed, followed by an approximately exponential decay higher in the freeboard. The model thus displays a property analogous to the "splash zone" observed at the top of bubbling fluidized beds. Agreement between the calculated and experimental profiles is best for the intermediate gas velocities, with the predicted flow rates generally larger than the observed values.

The fluxes of ascending and descending particles, and the particle density for the case with gas velocity equal to 0.53 m/s, are shown in Figure 3. The model predicts a maximum in the density near the bed surface, where most of the large particles change direction and return to the bed. Ascending particle flux and density become constant at a height of about 2 m, where only small particles, moving at constant velocity equal to $u_g - u_t$, continue upward. This point is the so-called "transport disengaging height".

## 3.0 Nitric Oxide Reduction in the Freeboard

### 3.1 The Mechanism of Nitric Oxide Reduction

The model for NO reduction in the freeboard has been under development for some time. An earlier version, having a less complete description of particle entrainment, was employed by Beer et al (21) for the prediction of NO profiles. Destruction of NO in the freeboard is assumed to occur by heterogeneous reactions with the coal char entrained from the bed:

$$NO + C = CO + 1/2\ N_2$$

$$2\ NO + C = CO_2 + N_2$$

Plug flow is assumed for the gas phase, and the char particle density is calculated using the model for particle entrainment described in Section 2, above. The rate of change of NO concentration with height is given by:

$$u_g \frac{dC_{NO}}{dZ} = - k A \rho_c(Z) C_{NO} \qquad 20)$$

where A is the specific surface area of char available for reaction, and $\rho_c$ is the calculated char particle density. Rate coefficients in the temperature range of interest have been reported by Chan (11).

$$k = 5.95\ T \exp(- E_a/R_o T)\ m/s$$

$$E_a = 81.6 \times 10^6\ J/kmol$$

$$T \leq 1016\ K$$

and by Song (22):

$$k = 4.1 \times 10^3\ T \exp(- E_a/R_o T)\ m/s$$

$$E_a = 136.8 \times 10^6\ J/kmol$$

$$T > 1016\ K.$$

The surface area assumed for the subbituminous coal char was based on the $CO_2$-BET surface areas reported for lignite and brown coal chars by Guerin et al. (23), Smith and Tyler (24), and Ashu et al (25). These workers reported specific surface areas ranging from 5 to 7 x $10^5$ $m^2/kg$ for particle sizes from 89 to 2000 μm. A value of 6 x $10^5$ $m^2/kg$ was used in the present calculations. The surface area of the bituminous char was taken near the lower limit of the range reported by Smith (26): 1.5 x $10^5$ $m^2/kg$. The char is treated as if all of its internal surface area were exposed to NO at the concentration and temperature found at the exterior of the particles (effectiveness factor of unity).

Nitric oxide profiles are found by integrating Equation 20, starting with the experimentally measured concentration at, or near, the surface of the bed.

### 3.2 Measurement of Gas Composition and Char Properties

Gas samples were withdrawn from the combustor through stainless steel probes. With the exception of the continuous sampling probe 4.1m above the distributor, all the probes were water cooled. Probes located in the bed were equipped with sintered quartz filters having pore sizes varying from 90 to 150 μm and sample openings 14.3 mm in diameter. Those located in the freeboard had quartz wool filters. The

accuracy of the reported axial positions of the probes is subject to an uncertainty of ± 40 mm; the probe tip locations relative to the centerline of the combustor varied from 50 to 170 mm. The gas sample continuously withdrawn at z = 4.1m passed through a KF 310 Heated Bypass Filter (Permapure Products, Oceanport, N.J.) to a heated line, and was dried by permeation distillation. This sample was analyzed using Beckman Model 865 non-dispersive IR analyzers for CO and $CO_2$, a thermoelectron Model 10 Chemiluminescent $NO_x$ analyzer, and a Beckman Model 755 Paramagnetic oxygen analyzer. The total sample flow rate was about $10^{-4}$ $m^3/s$ (NTP). The gas samples from the other probes were dried by permeation distillation, collected in 250 $cm^3$ bulbs for analysis on a HP 5830 A gas chromatograph. Hydrocarbons $C_1$ through $C_3$ were detected using flame ionization, and CO, $CO_2$, $N_2$, and $O_2$ by thermal conductivity. A thermoelectron Model 10 $NO_x$ analyzer, was also used to measure the NO mole fraction in this sample. The flow rate was 2 to 20 x $10^{-6}$ $m^3/s$ (NTP).

A gas sample withdrawn from the bed and mixed in a bulb is, in a simplified picture, a mixture of gases withdrawn from the emulsion and bubble phases. At typical operating conditions the composition is heavily biased toward the emulsion (Walsh et al (27)). In order to distinguish the NO contents of the emulsion and bubble phases, the length and diameter of the sample line to the NO analyzer were minimized so that a time-dependent NO mole fraction was observed. The measured NO mole fractions are shown in Figures 4-9, with bars indicating the maximum and minimum values recorded. An analysis by Pereira et al (28) concluded that, in the presence of excess air, NO is greater in the emulsion than in bubbles; and that under stoichiometric or sub-stoichiometric conditions the NO concentrations in the two phases are identical. To determine the mixed-mean NO mole fraction at the top of the bed, the average of the relative maxima observed in the time-dependent NO signal was assigned to the emulsion, and the average of the relative minima was assigned to the bubbles. The two averages were then weighted according to the relative flow rates of bubble and emulsion gas:

$$\bar{\bar{X}}_{NO} \simeq \bar{X}_{NO,max} \left[\frac{(1-\delta)u_{mf}}{u_g}\right] + \bar{X}_{NO,min} \left[1 - \frac{(1-\delta)u_{mf}}{u_g}\right] \qquad 21)$$

This weighted value is shown as a data point at the top of the bed in Figures 6-8; it is the initial value used when Equation 20 is integrated starting at Z=0.

Bed solid samples were withdrawn using a probe located 0.66m above the distributor. The probe was stainless steel, water cooled, and had a $N_2$ quench stream cocurrent with the sample. The outer and inner diameters of the probe were 44mm and 19mm, respectively. The extracted particles were separated from the gas stream in a water cooled cyclone and collected in a cooled vessel. The inert bed material was Ottawa silica sand. The coal char was separated from ash and sand particles collected in Runs C25-28 in order to determine the char particle size distribution. This was done by froth flotation. A representative sample of the bed solids was introduced into a flotation cell which contained a stirred kerosene-water emulsion together with 4-methyl-2-pentanol. The stirrer keeps the solids in suspension, breaks the kerosene into fine droplets, and disperses it uniformly. Nitrogen was introduced through a sintered stainless steel filter at the bottom of a cell, forming bubbles which adhere to the char particles and lift them up forming a froth, while the sand and ash particles were selectively depressed. The froth was collapsed in a filtering funnel and the char particles collected on the filter. The char was air dried for 24 hours and its size distribution determined using a Joyce Leobl "Magiscan" Image Analyzer. The size of each particle was defined as the diameter of the sphere with volume equal to the volume of the spheroid generated by rotation, about the major axis, of the ellipse defined by the length and breadth of the particle. An apparent char density, $\rho_{s,c}$, was determined from the calculated volume of the particles and the total mass of char; the results are given in Table 2. The char size distribution for Run C22 was found by sieving the bed sample and measuring the weight loss on ignition of each size fraction; in Run A14 the distribution was

assumed to be identical to that of the feed coal. The solid densities of the char in Runs A14 and C22 were estimated from published data.

Two coals were used in the present experiments: bituminous coal from the Arkwright mine in the Pittsburgh seam and subbituminous coal from the Colstrip mine in the Rosebud seam in Rosebud County, Montana. The composition of these coals is given in Table 1.

The size distribution of the fuel and bed particles were determined by sieve analysis. All of the size data for fuel, bed, and char particles were fit by log-normal distribution functions. The geometric means (mass basis) and standard deviation are listed in Table 2. The sizes were converted to a specific surface area basis for the computations. The fluidized combustor operating conditions and relevant experimental data are also listed in Table 2. The data from Runs A14 and C22 were first reported by Beer et al (19).

### 3.3 Comparison of the Measured and Predicted Nitric Oxide Profiles

The NO profiles predicted by the model are shown in Figures 4-9, together with the experimental data. When the calculation is started at the bed surface (solid line in Figures 4 and 5, dotted line in Figures 6-8) the agreement with experiment is good for Runs A14, C22, and C25; but very poor for Runs C26 and C28, in which there is a very rapid decrease in NO just above the bed, and a discrepancy of about 200 mole ppm between the predicted and observed NO mole fractions. There are not enough data to support a correlation of this behavior with operating conditions, however, it can be seen from the data in Table 2 that C26 and C28 have the lowest bed temperatures and lowest gas velocities. When calculation of the NO concentration for these two runs is started at the next higher data point, excellent agreement with experiment is obtained from that point upward (solid lines).

In Run C27 the combustor was operated using two-stage addition of the combustion air, with the secondary air injector located 1.7m from the distributor. The air/fuel ratio in the bed was sub-stoichiometric, giving very low NO near the top of the bed. The increase in NO mole fraction on addition of the secondary air indicates that some fuel nitrogen species, not detected in the NO mode of the $NO_x$ analyzer, are present in the gas leaving the bed. When the calculation of the NO profile is begun after mixing of the secondary air, the mechanism of the char entrainment/NO-char reduction model is still consistent with the experimental data.

The predictions of the combined model for char entrainment and NO reduction are in good agreement with the observed NO profiles at distances above 0.5m from the bed, in the absence of staged air addition; the model is not able to account for the rapid reduction of NO observed in the splash zone under some conditions. There are several phenomena, not incorporated in the model, which might account for a steep gradient in NO concentration in the splash zone. First, the reduction of NO may only be an apparent one due to uncertainty in the determination and weighting of the bubble and emulsion gas compositions. The estimate of the mixed mean gas composition in the bed (Equation 21) depends on the model used to estimate partitioning of the gas between bubble and emulsion. Other factors may contribute to the uncertainty in bed gas composition, for example, variation in the sample flow rate with the concentration of solids at the probe tip; and mixing of the sample in the probe, sample line, and reaction chamber of the NO analyzer. A second set of phenomena which might account for rapid reduction of NO in the splash zone is the alternate reaction pathways for destruction of NO, including reduction by CO, hydrocarbons, and $NH_3$. Chan (11) has shown that the NO-char reaction is enhanced in the presence of CO, the effect increasing with decreasing temperature. Reaction of NO and CO, catalyzed by coal ash, is also possible. Mori and Ohtake (29) measured an NO decomposition rate of 273 mole ppm/s.$m^2$ on alumina, in the presence of 1000 mole ppm CO at 1041 K. The rate of reaction was approximately first order in CO and zeroth order in NO, for NO above 300 mole ppm.

Nitric oxide reduction by methane, with reduction of up to 700 mole ppm NO in 0.5 s, was observed in $NO-CH_4-O_2-CO_2-Ar$ mixtures at 1323 K by Yamazaki et al (13). The temperature dependence of the rate is not reported so the possible contribution of this process at 1040-1100 K cannot be determined. Although the reduction of NO was only significant for $O_2/CH_4$ mole ratios of about 0.5 to 2.0, such conditions might exist locally during mixing of gases in the splash zone of the fluidized bed.

Reactions of NO with $NH_3$ such as:

$$NO + NH_3 = H_2O + N_2 + 1/2H_2$$

(Duxbury and Pratt (30)) are another possible contribution to the rapid NO disappearance at the top of the bed. Neither ammonia nor $NO_x$ was measured in the present experiments, so the contribution of this reaction cannot be precisely estimated. However, the increase in NO observed in run C27 on addition of secondary air is evidence that N-containing species other than NO may be present in the freeboard at least under sub-stoichiometric conditions. De Soete (31) determined an overall rate expression for the homogeneous reaction between NO and $NH_3$ giving $N_2$ from measurements in ethene/oxygen flames over the temperature range 1800 to 2400 K. The reaction is first order with respect to both NO and $NH_3$. The applicable temperature range is far from fluidized combustor conditions, however, the rate expression predicts an initial NO destruction rate of 140 mole ppm/s at 1040 K in a mixture containing 600 mole ppm each of NO and $NH_3$. It is possible that this reaction contributes to NO reduction in the splash zone. If it does contribute, the optimum (from the point of view of NO emissions) primary stoichiometric ratio in a configuration with staged air addition, may be one at which some NO is left unreduced at the top of the bed, providing a reactant for direct conversion of $NH_3$ to $N_2$ in the splash zone.

## 4.0 Conclusions

A mechanistic model for particle entrainment into the freeboard has been developed and used in conjunction with a chemical kinetic description of the NO-char reaction for prediction of the reduction of NO along the height of the freeboard in fluidized coal combustion. Bed conditions, including the mass fraction of char in the bed, are input to the model. Predicted NO profiles showed good agreement with experimental data obtained while burning bituminous and subbituminous coals under a variety of operating conditions. The steep reduction in NO observed in the splash zone immediately above the bed in some cases could not be adequately explained by the present model. This result points to the importance of the reactions in the splash zone, where it is thought that NO reducing reactions other than the NO-char reaction will have to be taken into account for satisfactory prediction of the NO profile under all conditions. The model is now in a form in which it can be integrated into system models for predicting NO emissions as a function of operating conditions.

## Acknowledgements

The development of the models for particle entrainment and nitric oxide reduction was supported by DOE under Contract No. EX-76-A-01-2295. The experimental work was supported by DOE under Grant No. DE-FG22-80PC30215, Dr. H. A. Webb, Project Manager.

Nomenclature

| | |
|---|---|
| $A$ | Specific BET surface area of char ($m^2/kg$) |
| $A_t$ | Cross sectional area of the bed ($m^2$) |
| $C_D$ | Drag coefficient |
| $C_{NO}$ | NO concentration ($kmole/m^3$) |
| $d_b$ | Bubble diameter (m) |
| $\bar{d}_B$, $\bar{d}_c$, $\bar{d}_f$ | Geometric mean diameters of bed particles, char particles, and fresh coal particles, respectively (m) |
| $E_a$ | Activation energy (J/kmol) |
| $E_d$, $E_u$ | Mass flow rates of downward and upward moving particles, respectively (kg/s) |
| $E_o$, $E_{o,c}$ | Initial entrainment rates of stone and char particles from the bed surface, respectively (kg/s) |
| $H_f$ | Total freeboard height (m) |
| $k$ | Rate coefficient (units variable) |
| $L_f$ | Expanded bed height (m) |
| $m_p$ | Mass of a single particle (kg) |
| $Q_b$ | Visible bubble volume flow rate ($m^3/s$) |
| $R_o$ | Gas constant = 8314 J/kmol · K |
| $R_b$ | Bubble radius (m) |
| $T$ | Temperature (K) |
| $T_B$ | Bed temperature (K) |
| $T_g$ | Gas temperature (K) |
| $u_b$ | Absolute bubble velocity (m/s) |
| $u_g$ | Superficial gas velocity (m/s) |
| $u_{mf}$ | Minimum fluidization velocity (m/s) |
| $u_t$ | Particle terminal velocity (m/s) |
| $v_d$, $v_u$ | Downward and upward particle velocities, respectively (m/s) |
| $v_s$, $v_{si}$ | Particle local velocity and particle initial velocity, respectively (m/s) |
| $\bar{v}_p$ | Root-mean-square particle initial velocity (m/s) |

| | |
|---|---|
| $X_k$ | Mole fraction of species k |
| $Y_c$ | Mass fraction of char in the bed |
| z | Distance above the distributor (m) |
| Z | Distance above the bed surface (m) |
| $\xi$ | Volume fraction of particles ejected per bursting bubble |
| $\varepsilon_{mf}$ | Bed voidage at minimum fluidization |
| $\rho(Z)$, $\rho_c(Z)$ | Local density of stone and char particles, respectively, at freeboard height Z, ($kg/m^3$) |
| $\rho_g$ | Gas density ($kg/m^3$) |
| $\rho_s$, $\rho_{s,c}$ | Solid densities of stone and char, respectively ($kg/m^3$) |
| $\delta$ | Bubble volume fraction |
| $\sigma_f$, $\sigma_B$, $\sigma_c$ | Geometric standard deviations of fresh coal particles, bed particles and char particles, respectively |

TABLE 1. ANALYSIS OF COALS

| Analysis (wt %) | Bituminous, Arkwright, Pittsburgh Seam | Subbituminous, Colstrip Mine, Rosebud Seam, Rosebud County, MT |
|---|---|---|
| Proximate | (as received) | (as received) |
| moisture | 1.6 | 19.19 |
| ash | 8.01 | 8.29 |
| volatile matter | 33.93 | 28.74 |
| fixed carbon | 56.46 | 43.78 |
| Ultimate | (daf) | (dry) |
| C | 76.36 | 67.80 |
| H | 5.23 | 4.45 |
| N | 1.47 | 1.00 |
| S | 2.61 | .59 |
| O | 5.26 | 15.91 |
| ash | - | 10.25 |

TABLE 2. OPERATING CONDITIONS AND EXPERIMENTAL DATA
(pressure = 101 kPa)

| Run Number | A14 | C22 | C25 | C26 | C27** | C28 |
|---|---|---|---|---|---|---|
| Coal Type | Bitum-minous | Subbitu-minous | Subbitu-minous | Subbitu-minous | Subbitu-minous | Subbitu-minous |
| $\bar{d}_f$ (μm) | 674 | 1000 | 1750 | 1750 | 2100 | 2100 |
| $\sigma_f$ | 1.87 | 1.8 | 1.83 | 1.83 | 2.12 | 2.12 |
| Stoichiometric air/fuel ratio | 1.19 | 1.22 | 1.21 | 1.25 | 1.02 | 1.07 |
| $T_B$ (K) | 1105 | 1134 | 1110 | 1050 | 1095 | 1040 |
| $T_g$(z=4.1 m) | - | - | 1002 | 932 | 1043 | 988 |
| $u_g$(m/s) | 0.98 | 1.46 | 1.00 | 0.80 | 0.94 | 0.86 |
| $X_{O_2}$ (z=0.9 m) (mole %) | 6 | 8 | 4.1 | - | 1.7 | 2.3 |
| $X_{O_2}$ (z=4.1 m) (mole %) | - | - | 3.2 | 4.0 | 3.5 | 1.5 |
| $X_{CO}$(z=0.9 m) (mole %) | 2 | 0.9 | 1.5 | 0.25 | 2.1 | 0.9 |
| $X_{CO}$(z=4.1 m) (mole %) | - | - | <0.005 | <0.005 | 0.11 | 0.14 |
| $X_{HC}$(z=0.9 m) (mole %) | 0.2 | 0.02 | 0.32 | 0.03 | 0.78 | >0.33 |
| $\bar{d}_B$ (μm) | 815 | 1300 | 800 | 800 | 760 | 720 |
| $\sigma_B$ | 1.42 | 1.32 | 1.44 | 1.44 | 1.35 | 1.37 |

Table 2 Cont'd

| Run Number | A14 | C22 | C25 | C26 | C27** | C28 |
|---|---|---|---|---|---|---|
| Coal Type | Bitum-minous | Subbitu-minous | Subbitu-minous | Subbitu-minous | Subbitu-minous | Subbitu-minous |
| $\bar{d}_c$ (μm) | 674* | 1123 | 2300 | 2300 | 2300 | 2400 |
| $\sigma_c$ | 1.87* | 1.41 | 1.55 | 1.54 | 1.52 | 1.55 |
| Apparent char solid density $\rho_{s,c}$ (kg/m$^3$) | 1400 | 1200 | 915 | 909 | 930 | 920 |
| Estimated bubble fraction, $\delta$ | 0.2 | 0.2 | 0.125 | 0.128 | 0.226 | 0.196 |
| Carbon mass fraction in the bed, $Y_c$ | 0.01 | 0.0012 | 0.0015 | 0.0011 | 0.0056 | 0.0023 |
| $\bar{\bar{X}}_{NO}$ at bed surface (mole ppm) | 380 | 500 | 717 | 561 | ~ 2 | 595 |
| BET specific surface of char (m$^2$/kg) | $1.5 \times 10^5$ | $6 \times 10^5$ | $6 \times 10^5$ | $6 \times 10^5$ | $6 \times 10^5$ | $6 \times 10^5$ |

*The char size distribution in the bed for Run No. A14 is assumed to be the same as the feed size distribution.

**Run No. C27 used staged addition of the combustion air.

References


1. F. J. Pereira, J. M. Beér, B. Gibbs, and A. B. Hedley, Fifteenth Symposium (Int'l) on Combustion, The Combustion Institute, Pittsburgh, PA, 1975, p1149.

2. B. M. Gibbs, F. J. Pereira, and J. M. Beér, Inst. Fuel, Symposium Series No. 1, Fluidized Combustion Paper D.6, 1975, pp1-13.

3. Y. Okada, J. Tatebayashi, and R. Yamamura, "Experimental Emission Control on Fluidized Bed Combustion of Coal," presented at AIChE Annual Meeting, San Francisco, CA, 1979.

4. S. E. George and J. R. Grace, AIChE Symposium Series, No. 176, Vol. 74, 1978, p67.

5. C. Y. Wen and L. H. Chen, The Proceedings of the Sixth International Conference on Fluidized Bed Combustion, USDOE, CONF-800428-Vol. 3, p1115.

6. M. Horio, A. Taki, Y. S. Hsieh, and I. Muchi, in Fluidization, Grace and Matsen, eds., Plenum, N.Y., 1980, p509.

7. F. J. Pereira and J. M. Beér, Deuxième Symposium Européen sur la Combustion, Orléans, France, 1975, p339.

8. T. Furusawa, D. Kunii, A. Oguma, and N. Yamada, Proc. Soc. Chem. Eng., Japan, 4 (1978)562.

9. J. M. Beér, A. F. Sarofim, L. K. Chan, and A. M. Sprouse, The Proceedings of the Fifth International Conference on Fluidized Bed Combustion, The MITRE Corporation, Vol. II, McLean, VA, 1978, p577.

10. D. Kunii, T. Furusawa, and K. T. Wu, in Fluidization, Grace and Matsen, eds., Plenum, N.Y., 1980, p175.

11. L. K. Chan, Kinetics of the Nitric Oxide-Carbon Reaction Under Fluidized Bed Combustor Conditions, Dissertation, MIT, Cambridge, MA, 1980.

12. A. F. Sarofim and J. M. Beér, Seventeenth Symposium (Int'l) on Combustion, The Combustion Institute, Pittsburgh, PA, 1979, p189.

13. S. Yamazaki, M. Hiratsuka, and Y. Fujitani, Combustion Science and Technology, 20 (1979)25.

14. P. M. Walsh, M. Nicastro, C. Sundback, J. M. Beér, W. R. Brooks, A. Dutta, C. J. Giallombardo, L. R. Glicksman, and M. C. Zhang, "Experimental Studies for Testing of Models and for Scale-up of Fluidized Bed Combustion," Technical Report for the Period April 14 to August 14, 1981, prepared for the Tennessee Valley Authority under Contract No. TV-55783, August 25, 1981.

15. T. Z. Chaung, "Further Studies on the Mechanistic Freeboard Model; Simulation and Measurements of Solid Flux in the Freeboard," In J. F. Louis and S. E. Tung, "Modeling of Fluidized Bed Combustion of Coal, Quarterly Technical Progress Report No. 20, prepared for DOE/Morgantown under Contract No. EX-76-A-01-2295, 1981.

16. S. Mori and C. Y. Wen, AIChE Journal 21 (1975)109.

17. L. R. Glicksman, J. Valenzuela, and W. Lord, "Fluid Dynamics Component Model," in "Modeling of Fluidized Combustion of Coal," J. F. Louis and S. E. Tung, Quarterly Tech. Progr. Report No. 12, Contract No. E(49-18)-2295, MIT, Aug. 1979.

18. J. F. Davidson and D. Harrison, Fluidised Particles, Cambridge University Press, 1963.

19. J. M. Beér, A. F. Sarofim, S. S. Sandhu, M. Andrei, D. Bachovchin, L. K. Chan, T. Z. Chaung, and A. M. Sprouse, "$NO_x$ Emission from Fluidized Coal Combustion," Final Report prepared for USEPA under Grant No. R804978020, 1981.

20. J. E. Mayo, "Determination of Solids Loading in the Freeboard Section of a Fluidized Bed Coal Combustor," B.S. Thesis, Dept. of Chemical Engineering, MIT, Cambridge, MA, 1980.

21. J. M. Beér, A. F. Sarofim, P. K. Sharma, T. Z. Chaung, and S. S. Sandhu, in Fluidization, Grace and Matsen, eds., Plenum, N.Y., 1980, p185.

22. Y. H. Song, Fate of Fuel Nitrogen During Pulverized Coal Combustion, Dissertation, MIT, Cambridge, MA, 1978.

23. H. Guerin, T. Siemieniewska, Y. Grillet, and M. François, Carbon 8 (1970)727.

24. I. W. Smith and R. J. Tyler, Combustion Science and Technology 9 (1974)87.

25. J. T. Ashu, N. Y. Nsakala, O. P. Mahajan, P. L. Walker, Fuel 57 (1978)250.

26. I. W. Smith, Fuel 57 (1978)409.

27. P. M. Walsh, A. K. Gupta, J. M. Beér, and K. S. Chiu, "Proceedings of the DOE/WVU Conference on Fluidized Bed Combustion System Design and Operation," Morgantown, WV, October 27-29, 1980, p455.

28. F. J. Pereira, J. M. Beér, and B. M. Gibbs, "Nitric Oxide Emissions from Fluidized Coal Combustion," presented at the Central States Section, The Combustion Institute, Spring Meeting, April 5-6, 1976.

29. Y. Mori and K. Ohtake, Combustion Science and Technology 16 (1977)11.

30. J. Duxbury and N. H. Pratt, Fifteenth Symposium (Int'l) on Combustion, The Combustion Institute, Pittsburgh, PA, 1975, p843.

31. G. G. De Soete, Fifteenth Symposium (Int'l) on Combustion, The Combustion Institute, Pittsburgh, PA, 1975, p1093.

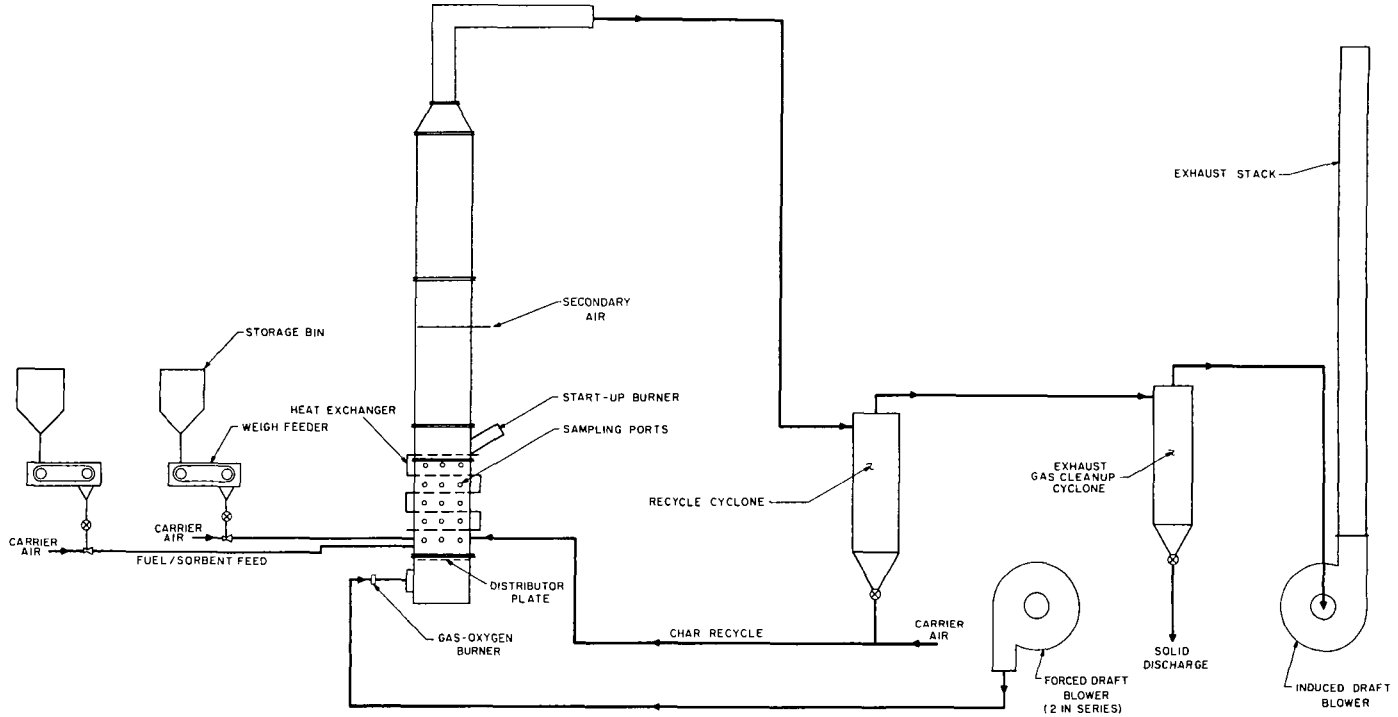


FIGURE 1. M.I.T. 0.6 m x 0.6 m, 500 kW (THERMAL) FLUIDIZED COMBUSTION RESEARCH FACILITY

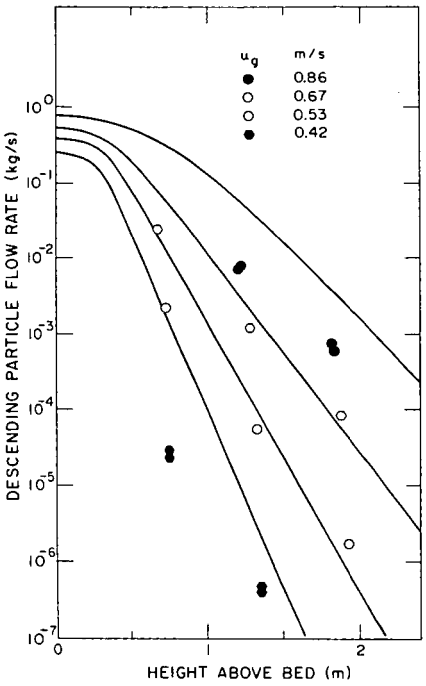


FIGURE 2. DESCENDING PARTICLE FLOW RATE VS. HEIGHT ABOVE THE BED. COMPARISON OF MODEL PREDICTIONS WITH EXPERIMENT.

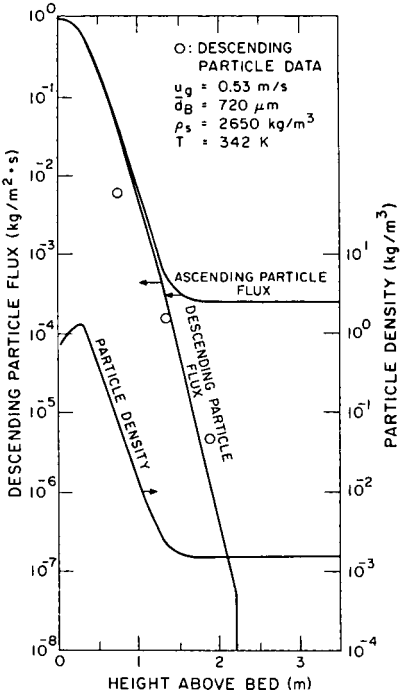


FIGURE 3. PARTICLE DENSITY, ASCENDING FLUX, AND DESCENDING FLUX VS. HEIGHT ABOVE THE BED.

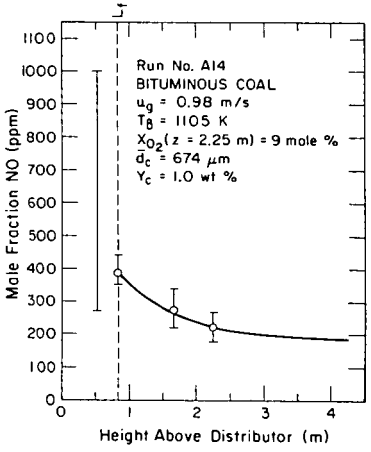


FIGURE 4. MOLE FRACTION NITRIC OXIDE VS. AXIAL POSITION
I MEASURED
— CALCULATED

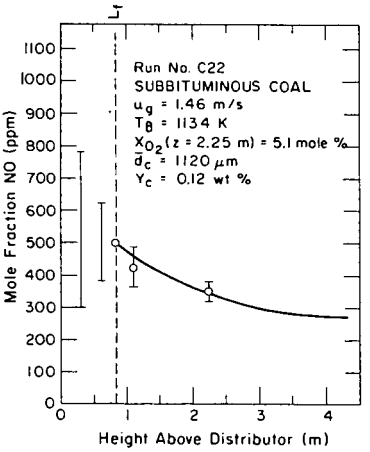


FIGURE 5. MOLE FRACTION NITRIC OXIDE VS. AXIAL POSITION
I MEASURED
— CALCULATED

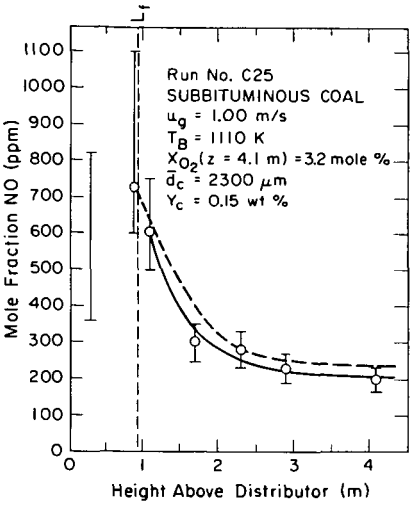


FIGURE 6. MOLE FRACTION NITRIC OXIDE VS. AXIAL POSITION
I MEASURED
CALCULATED

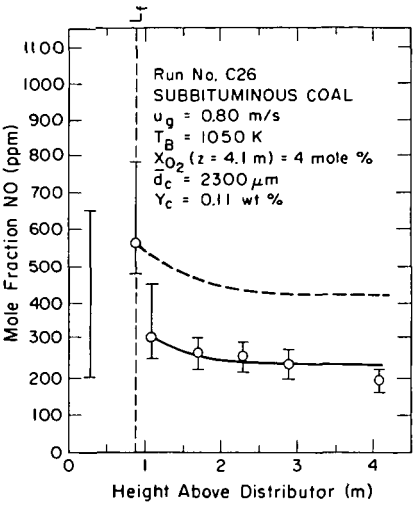


FIGURE 7. MOLE FRACTION NITRIC OXIDE VS. AXIAL POSITION
I MEASURED
CALCULATED

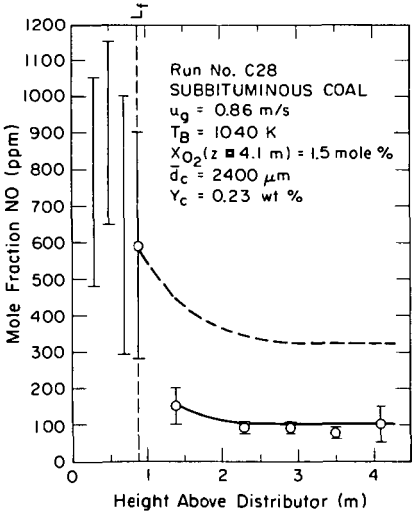


FIGURE 8. MDLE FRACTION NITRIC OXIDE VS. AXIAL POSITION
I MEASURED
CALCULATED

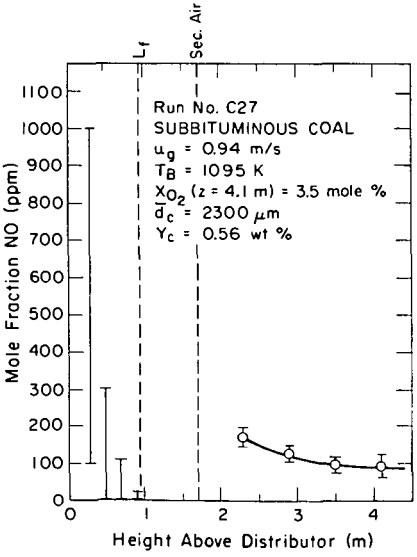


FIGURE 9. MOLE FRACTION NITRIC OXIDE VS. AXIAL POSITION
I MEASURED
CALCULATED